

A non-destructive analytic tool for nanostructured materials : Raman and photoluminescence spectroscopy

A. Singha, P. Dhar and Anushree Roy*

Department of Physics

Indian Institute of Technology,

Kharagpur 721 302, WB, India

Abstract

Modern materials science requires efficient processing and characterization techniques for low dimensional systems. Raman spectroscopy is an important non-destructive tool, which provides enormous information on these materials. This understanding is not only interesting in its own right from a physicist's point of view, but can also be of considerable importance in optoelectronics and device applications of these materials in nanotechnology. The commercial Raman spectrometers are quite expensive. In this article, we have presented a relatively less expensive set-up with home-built collection optics attachment. The details of the instrumentation have been described. Studies on four classes of nanostructures - Ge nanoparticles, porous silicon (nanowire), carbon nanotubes and 2D InGaAs quantum layers, demonstrate that this unit can be of use in teaching and research on nanomaterials.

*Electronic address: anushree@phy.iitkgp.ernet.in

I. INTRODUCTION

In the last couple of decades, research on semiconductors has dealt with, quite literally, novel phenomena in lower dimensions - two, one and zero. In such systems, electrons are confined in planes, lines and mathematical points, respectively. The dimension of these materials in the direction of confinement is in nanometer scale, hence the name nanomaterials. With miniaturization, quantum effects become significant and need to be analyzed in explaining their unusual physical properties. Such systems are, therefore, inherently quantum in nature. The 2D systems are called quantum wells, the 1D systems - quantum wires and the 0D systems - quantum dots. Interestingly, because of quantum effects, the properties of such materials are significantly different from the properties of the same material at either single molecule or bulk scale. Modern technology exploits this fact and uses these materials in diverse applications. For example, bulk CdS is yellow in colour. By changing the size of the nanoparticles of CdS, one can tune its colour. These coloured particles can then be used to tag biological molecules. Thus, nanoscience in conjunction with bioscience, can meet the challenge in scanning and identifying through thousands of genes and millions of proteins in search of new drugs and drug targets[1]. Research and development sectors all over the world embraced the use of nanomaterials based on silicon (Si) and germanium (Ge) for new and efficient optoelectronic device fabrication [2]. A new allotrope of carbon, the carbon nanotube (also called buckytube) has become a vital component in the fabrication of transistors [3] and flow sensors [4]. Apart from optoelectronics and bioscience, where nanomaterial applications are in abundant use, nanostructured materials are also important in information technology, integrated complex products such as hard disk drives that store information, silicon integrated circuit chips that process information in every Internet server and personal computer and in defence related applications [5, 6, 7]. There are others too. For example, a nanocomposite of epoxy layered silicate, can be employed as the primer layer of corrosion prevention coating in aircrafts and other high performance vehicles [8]. Thus, these new state of art materials play a pivotal role in facilitating improved as well as economic performance of a broad spectrum of instruments and devices, thereby uplifting the quality of life. A great emphasis is therefore needed in order to understand the fundamental properties of these low dimensional systems. Many research programmes, both in basic science and industry, have been initiated around the world over the last few years in an intense

effort to harness the potential of these materials for the generation of new technology.

Scientists need new and powerful analytic techniques to study these nanostructured materials, to discover the novel properties of these systems and to improve the materials for the future. Tools such as high-resolution transmission electron microscopy, scanning probe microscopy, x-ray diffractometry, photoluminescence spectroscopy and Raman and infra-red (IR) spectroscopy can be used to study different characteristics of these materials. Raman and IR spectroscopy measure vibrational levels of the molecules. These two techniques can be used complementarily, because, due to the differences in spectroscopic selection rules each is sensitive to different components of a given centrosymmetric molecule. For noncentrosymmetric materials these two techniques probe the same vibrational levels of molecules. However, there are many advantages of Raman spectroscopy over IR measurements - i. no tool-specific sample preparation is required (Nujol or KBr matrices are not used in Raman spectroscopy). Incident radiation can directly interact with the sample, ii. Raman does not suffer the material limitations of infrared spectroscopy since both glass and water exhibit minimal Raman spectral interference, iii. Raman bands are typically narrower than those observed in mid-IR spectra and can be used more readily for quantitative analysis, a fact to be discussed later in this article. Finally, Raman spectroscopy has a particular importance in the area of nanomaterial synthesis and their application in technology. This technique can therefore be uniquely placed to support the growing demand of understanding the properties of the novel materials of today.

In section II of this article, we have first discussed Raman scattering and Photoluminescence phenomena in brief along with how these two techniques can provide new and detailed information on the properties and quality of nanostructured materials. Section III describes the details of the spectrometer, which we have assembled, to carry out the above studies. Section IV deals with the calibration of this spectrometer and the study of standard samples. Using the above instrument, Raman and photoluminescence spectroscopic studies on different nanostructured materials are discussed in section V. Finally, in section VI we summarize our results and make a few concluding remarks.

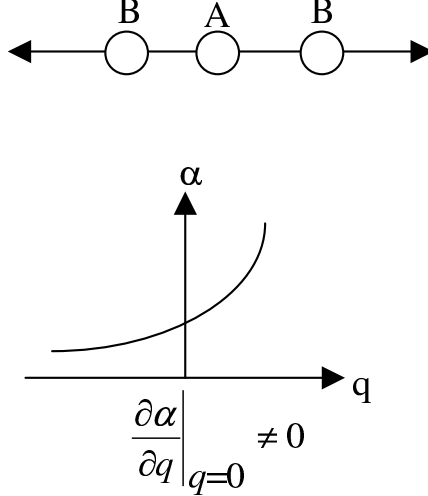


FIG. 1: Dependence of $\partial\alpha/\partial q$ on the normal coordinate of vibration for a AB₂ type molecule

II. RAMAN AND PHOTOLUMINESCENCE SPECTROSCOPY : BASICS

A. Raman spectroscopy

Inelastic scattering of light was first predicted in 1923 by A. Smeckal [9]. However, it was not until 1928 that Sir C.V. Raman carried out the first set of experiments, which confirmed the prediction and led to the Nobel award in 1930 [10]. Unlike Rayleigh scattering [11], which is elastic scattering of light, Raman scattering is an inelastic process caused by some quasi excitations of the medium. These excitations can be vibrational modes in a molecule, phonons in a crystal, plasmons, single particle electronic excitation, magnons etc [12, 13].

Classically, Raman scattering can be explained by a time varying polarizability of the molecule modulating an optical response. When a molecule is subjected to the electric field $\mathbf{E} = \mathbf{E}_0 \cos \omega t$ of a beam of electromagnetic radiation, the dipole moment \mathbf{p} of the molecule is given by

$$\mathbf{p} = \mu_0 + \tilde{\alpha} \mathbf{E} \quad (1)$$

where μ_0 represents the permanent dipole moment, while $\tilde{\alpha} \mathbf{E}$ is the induced dipole moment. In general, the polarizability is represented by a rank two tensor, α_{ij} . The structure of α_{ij} depends on the symmetry of the molecule. For small vibrations the normal coordinates $q_n(t)$ of the vibrating molecule can be approximated as $q_n(t) = q_{n0} \cos(\omega_n t)$, where q_{n0} is the amplitude and ω_n , the vibrational frequency of the n th normal mode. The total dipole moment is then given by

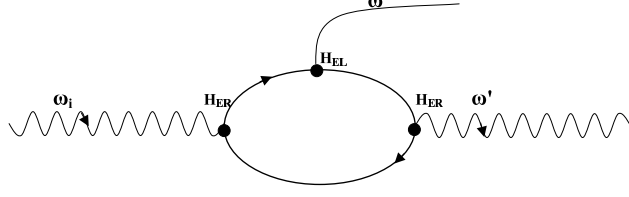


FIG. 2: Schematic of Raman scattering process

$$\begin{aligned}
 \mathbf{p} = & \mu_0 + \alpha_{ij}(0)E_0\cos(\omega t) + \sum_{n=1}^Q \left(\frac{\partial \mu}{\partial q_n} \right)_0 q_{n0}\cos(\omega_n t) \\
 & + \frac{1}{2}\mathbf{E}_0 \sum_{n=1}^Q \left(\frac{\partial \alpha_{ij}}{\partial q_n} \right)_0 q_{n0}[\cos(\omega + \omega_n)t + \cos(\omega - \omega_n)t]
 \end{aligned} \quad (2)$$

where the Taylor series expansions in q_n , for μ and $\tilde{\alpha}$ have been used and only first order terms retained. The second term describes Rayleigh scattering, the third term the Infrared spectrum and the fourth term, the Raman scattering process. Thus, for a mode of vibration of a molecule to be 'Raman active', the necessary criterion is $\frac{\partial \alpha}{\partial q}|_{q=0} \neq 0$ [Fig. 1].

In microscopic theory, inelastic scattering of an incident photon by phonons, for example, in a crystal is defined by a third order interaction process between electron and radiation (denoted by the interaction Hamiltonian H_{ER}), electron and lattice (H_{EL}) [14]. Fig. 2 illustrates the Raman scattering process in terms of these elementary interactions. An optical photon (frequency ω_i and wavevector \mathbf{k}_i) cannot interact with the lattice directly; rather it interacts with an electron via the electron radiation interaction. An electron-hole pair is created in this process. After creating (or annihilating) a phonon of frequency ω (and wavevector \mathbf{k}) via electron-lattice interaction, this electron recombines with the hole via electron-radiation interaction. The interaction vertices (denoted by the black dots in Fig. 2) makes the overall process of third order (i.e. second order in the electron-radiation interaction and first order in the electron lattice interaction). If the scattered phonon frequency is ω_s (and wavevector \mathbf{k}_s), energy and wavevector conservation lead to

$$\omega_i = \omega_s \pm \omega \quad \mathbf{k}_i = \mathbf{k}_s + \mathbf{k} \quad (3)$$

If ω_s is smaller (larger) than incident photon frequency, ω_i , it is called Stokes (Anti-Stokes) scattering. Change in the incident photon frequency (often expressed in wavenumber, cm^{-1}), $\omega_i - \omega$, is called the Raman shift.

The Raman scattering cross-section can be shown to be proportional to (i) ω_s^4 and (ii) the second order term of the polarizability tensor ($\alpha_{ij,n} = \left[\frac{\partial \alpha_{ij}}{\partial q_n} \right]_{q=0}$) associated with the electrons in the material [14] : (i) implies that for smaller wavelength the spectral lines are more intense. It is also easy to note that because of (ii) Raman scattering is a very weak process and therefore not easy to detect without specific experimental arrangements.

Unlike bulk systems, phonons are typically confined in nanomaterials. As we shall see below, for low dimensional systems, Raman spectroscopy can be used to investigate these confined and surface/interface phonon modes. In addition, it can also be used to study structure, quality and thermodynamic properties of materials. We now briefly outline these aspects.

Confined phonon modes : An acoustic phonon in a bulk crystal is usually described by the vibrational theory of a continuous elastic body (all the atoms in a crystal move together, as in a long wavelength acoustic vibration). On the other hand, in zero dimensional systems, these modes arise due to elastic vibrations of a homogeneous elastic body as a whole (that is why it is also called particle mode). Under stress free boundary condition, it gives rise to two acoustic modes : spheroidal (vibration with dilatation) and torsional (vibration without dilatation). Spheroidal modes are Raman active and the frequencies of these modes are inversely proportional to the size of the particles [15, 16, 17]. Because of very low frequency the acoustic modes for the bulk systems cannot be observed by Raman measurements, but for low dimensional systems they appear in the measurable frequency region (below 100 cm^{-1}) of the Raman spectrum. Furthermore, in two dimensional systems, we observe a new phenomenon - the folding of acoustic phonon modes. A 2D quantum well structure is formed by layered growth of two semiconductor species with different band gap energies. Acoustic phonons in such a structure overlap in frequency and can propagate normal to the interface, i.e. along the growth direction. The folding of acoustic phonon modes in a layered structure is understood using either the (i) linear chain model (LCM) [18] or (ii) the effective continuum model (ECM) [19]. We briefly describe (i) here. Imagine a linear chain of atoms representing the layered structure across the interface. For, example, in a Ga-As, Al-As layer the chain contains alternating Ga, As and Al atoms. The elastic coupling between Ga, As is obviously different from that for Al, As. The set of equations governing the displacements of each atom forms a coupled oscillator system. For individual layers one can work out the solutions. Across each layer of different constituents one needs to match the forces. The end

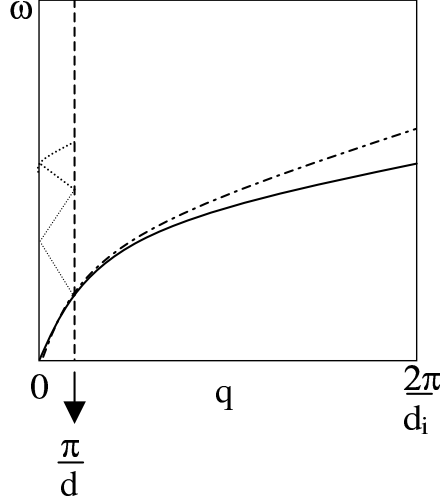


FIG. 3: Schematic illustration of the folding of acoustic phonon (dotted line) within mini zone boundary, π/d (dashed line). The bold line and the dashed-dotted lines are the acoustic phonon dispersion curves (ω - q , $i=1,2$) for the two components of the layered structure

result of such matching reveals the folding of the phonon modes at the new zone boundary, π/d , where $d=d_1+d_2$ (thickness of the layers of the components). This is schematically shown in Fig. 3. In (ii) one assumes an elastic continuum with different sound velocity and density on either side of the boundary separating the layers. The solution of the wave equation and its derivative are matched at the boundary. The folding of acoustic phonons can also be explained in this 'continuum' framework, where the qualitative result remains the same as in LCM. These typical features of the confined acoustic phonons in low dimensional systems can be observed and quantified successfully through Raman measurements. The interested reader can look up [20] for a lucid discussion on these aspects.

In contrast to the acoustic phonons, the optical phonon frequencies of the two constituent materials of the layered structure may overlap in some region or may not overlap. In the former case, the optical phonon modes can be described by folding into the new mini zone boundary, π/d , similar to acoustic phonon modes. In the latter case, phonons cannot propagate in the growth direction, hence they are confined in each layer. Confinement of optical phonon modes in low dimensional systems will be discussed later in section V of this article. We note here, that the propagation of acoustic phonons is sensitive to the periodicity of the well-structure, while optical phonons are sensitive to interface properties of the each

individual quantum well.

Interface and surface phonons : As mentioned before, Raman spectroscopy can be used to study interface and surface phonons in nanomaterials [21, 22, 23]. The long wavelength optical modes, which correspond to coupled excitations of phonons and photons, are also known as polaritons. Their frequencies are complex, the imaginary parts arise from both anharmonicity and radiative damping. Detailed analysis shows [21] that the polaritons of longitudinal electric type are bulk modes, whereas the polaritons of transverse magnetic type are surface modes. From the coupling of the electric field of the photon to the dielectric polarization of the transverse optical phonon, the dielectric function is obtained as

$$\epsilon(\omega) = \epsilon(\infty) \left(\frac{\omega_L^2 - \omega^2}{\omega_T^2 - \omega^2} \right) \quad (4)$$

ω_L and ω_T are longitudinal optical (LO) and transverse optical (TO) phonon frequencies, respectively. $\epsilon(\omega)$ is negative when $\omega_{LO} < \omega < \omega_{TO}$. For a plane wave propagating in the x-direction in a bulk crystal, the temporal and spatial variation of the wave is described by the factor $\exp[i(kx - \omega t)]$. In the frequency range for which $\epsilon(\omega) < 0$, k is imaginary ($k = \sqrt{\epsilon(\omega)}$) and the wave decays exponentially. Therefore, in this frequency range, an electromagnetic wave cannot propagate much in the bulk crystal. These surface modes in the bulk sample are so weak that they cannot be detected by Raman measurements. In contrast, because of high surface to volume ratio, these modes (which involve interface modes as well) appear in low dimensional systems and are detected easily by Raman scattering.

Structure and quality of the material : Raman measurements also provide detailed information on the structure and quality of low dimensional materials. The reason behind is that lattice vibration is very sensitive to nearest neighbour interaction and therefore can efficiently probe crystal structure and quality in extremely small scale (of the order of lattice spacing). For example, investigations on longitudinal optical (LO) phonons in semiconductors via Raman spectroscopy provide significant information about the strain, defects and disorder in these materials [24, 25]. Measurement of the Raman spectrum in these systems tells us about the microstrain in semiconductors under stress. This inherent stress at the interface causes the polarization dependent splitting and/or shift of the Raman line, which vary linearly with the stress. Raman shift due to the hydrostatic component of the strain yields a value for the Grüneisen parameter (average value of change in vibrational frequency of the atoms in a crystal per unit dilation) for the new material [26, 27].

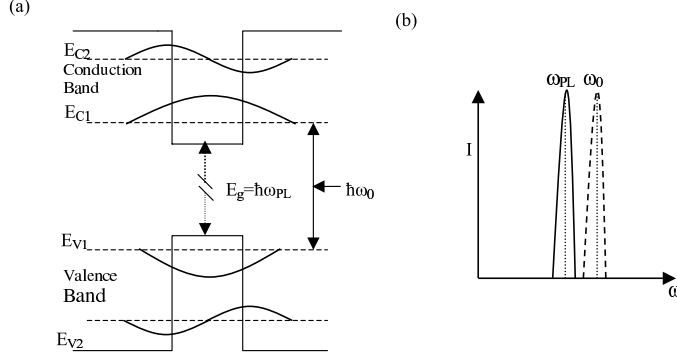


FIG. 4: (a) The electronic transition between the quantized levels E_{c1} to E_{v1} in a semiconductor low dimensional system in comparison with PL energy of the bulk system (b) corresponding photoluminescence intensity as a function of frequency for low dimensional system (dotted line) and for the bulk system of same material (solid line)

Phase transitions: An additional thermodynamic aspect is phase transitions, which can play an important role in device fabrication. For instance, the current injected laser diodes based on GaN require suitable thermodynamic properties for their stability and resistance to degradation under conditions of high electric currents and intense light illumination [28]. Phonons are primary excitations, which influence the thermodynamic behaviour. The pressure dependence of the optical mode energies can be related to homogeneous shear strain caused by a phase transition [29]. This shear strain in the crystal can be measured from the change in frequency of the Raman shift. The phase transitions in a material under different conditions can be identified from the discontinuities in the Raman peak positions, as well as from the changes in the number of observed Raman lines [30].

In summary, the crucial knowledge of strain, disorder, phase in a material can be obtained with a fair amount of precision through specific features of the Raman shift.

B. Photoluminescence

The above discussion tells us that Raman scattering essentially probes the electron-lattice interaction. On the other hand, photoluminescence is directly related to electronic structure and transitions. Differences in the electronic behaviour between bulk and low dimensional semiconductors arise due to the difference in the electronic density of states. For example, density of states of electrons, $N(E)$, of a bulk semiconductor has a continuous dependence

$N(E) \sim E^{1/2}$, whereas in 2D semiconductors it has a step-like dependence with energy. In 1D semiconductor structures it diverges with energy as $E^{-1/2}$ and for 0D semiconductor it is a delta function of energy. In semiconductors, electrons in the valence band absorb photons and get lifted into the conduction band everywhere, leaving holes in the valence bands. In a bulk sample, this occurs provided $\hbar\omega \geq E_g$, where E_g is the band gap of the semiconductor and ω is the frequency of incident photon. Some of these excited electrons lose their energy by nonradiative transition. It is then possible for an electron to fall from conduction band into the holes in the valence band by a radiative transition process. Usually the lowest levels are seen in PL spectrum and the emitted PL frequency, $\omega_{PL} < \omega$. Thus, PL spectrum of a bulk semiconductor, in general, corresponds to its band gap. In low dimensional systems, because of the quantization of energy levels in the conduction and valence bands (increase in bandgap) the frequency of PL emission, ω_0 , corresponds to the transition of excited electrons from the lowest state in the conduction band (E_{C1}) to the lowest state in the valence band (E_{V1}) [Everything is upside down in the valence band, as shown in Fig. 4. Since $\omega_{PL} < \omega_0$ PL peak in these systems shifts from that in corresponding bulk materials. The schematic of this phenomenon is illustrated in Fig. 4. The process can be direct or indirect depending on the gap energy. The characteristic shift of the band gap with decrease in size of the clusters can be studied from the blue-shift in PL peak position [31]. This technique has been shown to be useful in the study of quantum confinement of electrons in low dimensional systems.

Due to change in band gap some of these nanostructured materials can have tunable light emission, where the tuning depends on the size of the nanostructures. These have many potential applications in optoelectronic devices [2]. PL spectroscopy also yields information on the surface state density through intensity variations [32] and width of the spectrum. Surface states are caused by the interruption of the periodical arrangement of the atoms and by the deposition of impurities at the surface. Because of large surface to volume ratio this effect is more pronounced in nanoparticles. Thus, PL spectroscopy offers a tool for improving our understanding of the compound semiconductor surface. Moreover, for device fabrication using semiconductor low dimensional systems, such studies demonstrate the feasibility of improved technology. For example, the efficiency of solar cells is limited by non-radiative recombination occurring in the bulk via defect states or at the surfaces via surface states. PL spectroscopy also gives us information on band bending [33], surface related transitions [34] and near-surface bulk properties [35].

| Raman spectroscopy | Photoluminescence spectroscopy |
|--|--|
| Interface properties of individual quantum well | Origin of luminescence in quantum systems |
| Periodicity of the quantum well structure | Electronic states of the materials |
| Size of the quantum dots from the confinement of phonons | Electron hole exchange interaction |
| Local field effects in quantum dots embedded in a matrix | Surface state density -provides information for compound semiconductor surface |
| Defect/disordered states in the quantum structures | Surface related electronic transition |
| Microstrain in the quantum systems | Electronic band bending |
| Grüneisen parameter of the low dimensional systems | Near surface bulk properties. |
| Thermodynamic properties, like phase transition in the materials | |
| Dopant concentration in semiconductor quantum dots | |

TABLE I: Brief listing of information on the nanomaterials obtained from Raman and PL spectroscopy

Thus, Raman and PL spectroscopy yield structural and dynamic information on materials at the molecular level. Unfortunately, modern commercial spectrometers are highly expensive and becoming an option for the budget in many research labs. In this paper, we present the design of a relatively low cost Raman spectrometer, which can ideally be used to study today's state of art nanomaterials. Table I briefly summarizes how Raman and PL spectroscopy can be used to study nanomaterials.

III. INSTRUMENTATION

As we mentioned before, being a third order interaction process Raman scattering is an extremely weak phenomenon. Moreover, because of very low volume fraction of the materials in nanostructured systems, it is often quite difficult to get a Raman signal without damaging the sample by a high power laser. Thus, one needs a clever choice of the optics to collect scattered light from the sample. The low cost spectrometer, described here is useful

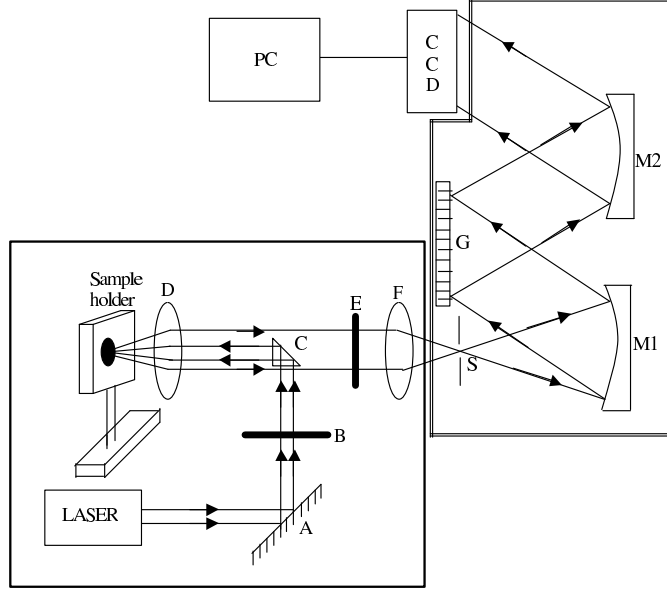


FIG. 5: Schematic diagram of the Raman set-up. The actual size of the prism (C) is much smaller.

both for Raman and PL measurements. The instrument consists of an inexpensive single Monochromator with open electrode CCD detector and 100 mW air cooled Argon ion laser source. The collection optics is home-built. Schematic diagram of the spectrometer is shown in Fig. 5. The details of the instrument is discussed below.

Excitation source : In the pre-laser era the main drawback was the lack of a sufficiently intense radiation source to detect the weak signal from inelastic scattering. Introduction of lasers has revolutionized this classical field of spectroscopy. To get detectable scattering intensity one usually uses either water cooled high power (Watt) lasers, which are not only expensive, but also difficult to maintain. One needs good infrastructure like stable power and water supply to run it efficiently. We have used a single line polarized (TEM_{00} mode) 100 mW air cooled argon ion laser of wavelength 488 nm, Model no. 177-G12 from Spectra Physics, as an excitation source. Because of vacuum sealing and factory aligned cavity optics, an air-cooled laser does not require any adjustment or regular cleaning; this eliminates costly system downtime. We have used a 5KV UPS for stable power supply for the laser and we obviously do not need constant water circulation to run this laser. This laser is economic compared to a high power laser, easy to maintain and it serves our purpose.

Collection Optics: In the usual commercial set-ups, low power (mW) lasers are used along with a MicroRaman system to record the weak Raman scattering signals. The collection op-

tics in such a set-up consists of expensive microscope objective along with a notch filter[36]. MicroRaman spectrometer also requires crucial alignment of the Monochromator and detector. In contrast, in our set-up, except a notch filter, we have used simple in-expensive optical components (mirror, lens and prism) for collecting the Raman signal from the sample and directing it to the Monochromator. The schematic diagram of the collection optics is shown in the square marked (single line) area in Fig. 5. It is easy to align all the components for collection of the spectrum. For stability and alignment of the system we have kept the optical components on a breadboard. Using a mirror (A), light from the laser is steered to plasma filter (B) [Omega optical Inc.] and then to a tiny right angle prism (C), where it bends through 90 degree. This light is focused on the sample by a Nikon camera lens (D) of focal length 55 mm. The scattered light is collected by the same lens, then it passes through a holographic Super Notch filter (E) [Model no. 1495-488-SNP from Keiser Optical system Inc.]. This notch filter is used to cut off the Rayleigh line from the scattered light. After passing through the notch filter the scattered light is then imaged on the entrance slit S of the Monochromator using a collecting and focusing lens (F) of focal length 55 mm.

For high efficiency of the instrument the selection of the above optical components has been made very carefully based on detailed estimation of several parameters, in particular - focal length of the lens, size of the prism, reflectivity of the mirror. We have used high quality front face reflecting mirror (A) of reflectivity 98% at 488 nm for steering of the beam. We have chosen a very tiny prism (C) of flint glass and appropriate holder so that the scattered light from the sample ($1 \text{ in } 10^5$) is not hindered. The Abbe number of the prism is 36.37. Inverse of Abbe number is called the dispersive power (does not play a vital role in our set-up) of the prism. In our system, the scattered light is collected in 180 degree scattering geometry. This set-up does not require any vibration isolation table. A heavy wooden table is providing a reasonable stability to the set-up by eliminating spurious vibrations appreciably.

Notch filter : In the scattering process strong elastically scattered Rayleigh background often masks weak inelastically scattered Raman signals. To remove this Rayleigh background, usually high-cost double or triple Monochromator is used as dispersive unit. These Monochromators are expensive and a large number of optical components in the dispersive unit attenuate the scattered light quite significantly. To get the appreciable intensity of the inelastically scattered light it is essential to use high power lasers as an excitation source

with double/triple Monochromators. The background due to Rayleigh scattering cannot be suppressed efficiently by a single Monochromator, especially at low wavenumbers. But, the combination of single stage Monochromator with Rayleigh line rejection filter, i.e Notch filter, of large optical density at the laser frequency offers an efficient and low cost alternative. The super notch filter, which we have used, has an optical density >6.0 at 488 nm, spectral band width of 350 wavenumber and spectral edgewidth of ~ 150 wavenumber.

Monochromator : We have used a single stage ISA TRIAX 550 Czerny-Turner Monochromator as the dispersive unit. The schematic diagram of the optics of grating Monochromator is shown in the square marked (double lines) area in Fig. 5. The slit S is placed in the focal plane of a concave mirror M1. Mirror M1 and M2 image the entrance slit on the detector. It uses 76mm \times 76mm holographic grating (1200 rulings/mm) for dispersion of the spectral line. The density of the groove at longer wavelength provides the best resolution of the spectrometer as 0.025 nm. The large grating provides very good light collection with f/6.4 aperture. The width of the slit S can be varied from 2 μm to 2000 μm . This Monochromator has focal length 0.55 m. It can be used for both Raman and PL measurements.

Detection system : To measure very weak signals Charge Coupled Device (CCD) is often used as a detector at the exit slit of the Monochromator of a Raman set-up. Multichannel CCD helps one to collect more scattered light signals for a wide spectral window in shorter time than what can be done by a Photomultiplier tube (PMT). Thus, using this device a very weak signal can be collected with help of a very long integration time. Depending on design and operating parameter there are three kinds of CCD detectors available - i. Front illuminated ii. Back thinned iii. Open electrode. The optimum choice of a CCD detector depends upon i. wavelength range of interest ii. amount of anticipated signal iii. spectral coverage and resolution. We have used high performance thermoelectrically cooled, of 1024 \times 256 pixel, front illuminated open electrode (OEL) CCD chip. Though the quantum efficiency of this kind of CCD detector is only 53% in the visible and near infra-red (NIR) range (400 nm - 900 nm) and 30% in UV region compared to quantum efficiency of 90% (only in visible range, starts to fall off above 800 nm and below 450 nm) in back thinned CCD chips, we have chosen this particular kind of detector for the following reasons: A) unlike back-thinned and front illuminated CCD detectors the dynamic range of OEL CCD is not a limiting factor as it has an average quantum efficiency of 40% with relatively large response over 200-900 nm. The spectrometer with this detector can be easily

used to study PL in different semiconductor materials, Raman scattering from biological samples (which usually needs detection of light in infra-red/NIR regions) using appropriate laser source. Moreover, though the quantum efficiency of OEL CCD is comparatively low, one can overcome this drawback by collecting weak signals with long integration time, B) when back thinned CCDs are used in NIR region, etalonic effect appears due to interference induced by reflection of some wavelengths at the boundaries of the silicon layers in the chips. This results in oscillations superimposed on collected CCD data. Etalonic effect can be minimized by reducing the size of the image focused onto the detector or by changing the central wavelength of the acquisitions. However, this effect cannot be totally suppressed. With OEL one can completely avoid such problem, C) OEL CCD detectors are cheaper (nearly half the price) compared to back-thinned CCD detectors.

We believe that OEL CCD detectors are good enough for Raman and PL measurements, which we are aiming at. We have measured very weak Raman signals from nanomaterials using this detector (discussed later).

Interfacing, data acquisition and analysis: Data acquisition is done by interfacing CCD and computer via IEEE card no. P/N 973027. For data acquisition and data manipulation we have used a Windows based programme Spectramax[37]. This commercial programme is also capable of fitting the Raman peaks by non-linear curve fitting programme, data editing, conversion of units, calculation of peak area and line width. Using the same software one can also collect raw data in ASCII form for further analysis after acquisition.

Instrumentation particularly ideal to study nanomaterials: The intensity of inelastic scattered signals from nanomaterials are extremely weak. The use of double/triple Monochromator causes loss of signals in a large amount due to presence of large number of the optical components in the spectrometer. To compensate this loss the use of high power laser is also not an ideal solution. High power density of the laser on the focused spot can cause unwanted phase transitions in the material. Use of single Monochromator with notch filter is an intelligent solution to above problems. With multichannel CCD detector one can use a very long integration time to collect very weak Raman signal from the sample for a wide spectral window.

Drawback of the present set-up : Besides various advantages as discussed in this section, the above Raman set-up has the following disadvantages 1. Resolution of single stage Monochromator is poor compared to double/triple stage Monochromator. 2. Notch filter

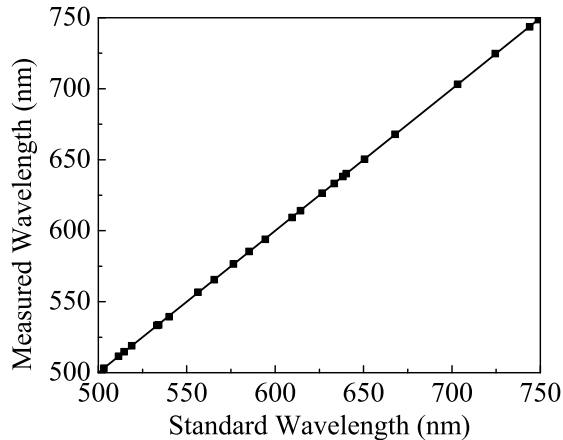


FIG. 6: Plot of observed and standard Neon peaks showing linear correlation

cut off is at 150 cm^{-1} . Using this instrument it is not possible to record Raman spectrum below this wavenumber. Thus, this set-up is not appropriate for studying acoustic phonons in semiconductors and optical/acoustic phonon modes in metallic systems. 3. The notch filter needs very careful handling. It is extremely sensitive to atmospheric conditions, humidity and temperature.

IV. CALIBRATION

The first step after installation of the instrument is to calibrate and to study a few standard samples.

A. Calibration of the System

The calibration of the Monochromator has been carried out using a Neon lamp. The entrance slit of the Monochromator was opened $50 \mu\text{m}$ for the calibration. At this slit width the resolution of the instrument is 0.03 nm (1 cm^{-1}). The spectrum was obtained in the wavelength range 500 nm - 750 nm . A plot of the measured wavelength and the standard wavelength is shown in Fig. 6. The linear correlation between these two measures the accuracy of the measurement by the Monochromator.

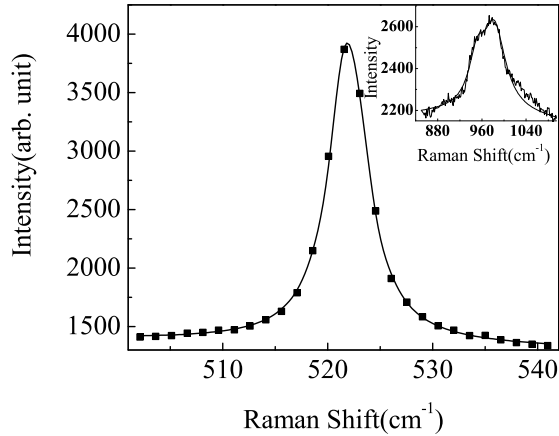


FIG. 7: First order Raman spectrum of Silicon. 2nd order spectrum is shown in the inset.

B. Standard Sample Study: Solid And Liquid

Subsequent to the installation and calibration of the instrument a number of standard samples have been studied, which include solids and liquids. It is important to state here what we measure. Given a sample, its Raman spectrum is shown as a plot of intensity of scattered signal vs. Raman shift. Unless otherwise mentioned, in all figures the filled squares and the bold line represent the experimental data points and the fitted curve, respectively. For all the measurements, reported in this article, we have used the entrance slit width of the Monochromator as $50 \mu\text{m}$.

Silicon: We have chosen silicon as a standard solid sample. Raman spectrum of a polished Silicon wafer (001) is shown in Fig. 7. The spectrum was taken with 80 mW power of the laser at laser head and $50 \mu\text{m}$ slit-width. By fitting the experimental data points with Lorentzian line shape the first order Raman line of Silicon is obtained at $521.9 \pm 0.01 \text{ cm}^{-1}$. The expected value for the same from the literature is 522 cm^{-1} [38]. From the data analysis the width of the peak at half maxima (FWHM) is 4.4 cm^{-1} . Weak 2nd order TO mode of Si, measured by our instrument, has been shown in inset of Fig. 7. [Zig-zag line is the measured spectrum]

Benzene: Raman spectrum of Benzene in the range 975 cm^{-1} - 1010 cm^{-1} is shown in Fig. 7. We have fitted this peak with a Lorentzian and the peak position is obtained at $992.3 \pm 0.03 \text{ cm}^{-1}$. The corresponding peak due to C-C vibration is expected at 992.36 cm^{-1} [39].

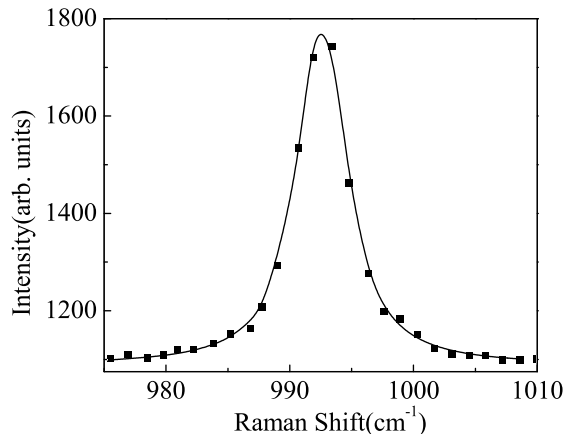


FIG. 8: Raman spectrum of Benzene.

Thus, our measurement is in good agreement with the data available in the literature.

Equipped with a calibrated instrument, tested with standard samples, we now move on to demonstrate how we can use it to study nanomaterials.

V. STUDIES ON NANOMATERIALS

In the introduction of this article we said that low dimensional systems, where the quantum confinement appears at the nanoscale can be of dimensions - two, one or zero. Below, we provide an example of each of these low dimensional systems. Most of the samples have been prepared by us. We investigate the optical properties using PL and Raman measurements and point out what can be achieved by such studies.

A. Zero Dimensional System

Ge implanted in Si: Semiconductor doped glasses show interesting optical properties as a result of quantum confinement of electron and hole wave functions in the embedded semiconductor nanocrystals [40, 41]. Light emission from Ge nanocrystals embedded in SiO₂ matrix is becoming an expanding field of interest [42] because of their potential use i. as optoelectronic emission devices directly coupled with Si integrated circuits [43] and ii in memory device applications [44]. A lot of effort is being made in order to improve the

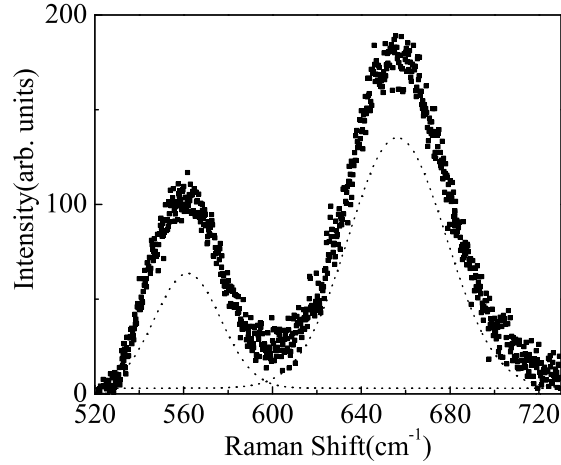


FIG. 9: Photoluminescence spectrum for Ge in Ge ion implanted Si/SiO₂ sample.

performance of these devices. In this context, the study of optical properties, as we shall see, has a role to play. We have studied the optical properties of Ge clusters in Si/SiO₂ matrix, prepared by low energy ion-implantation [45]. This technique is considered as one of the promising tools to synthesize embedded nanocrystals, as it can control the size distribution and depth profile of the particles within the matrix efficiently. ⁷⁴Ge⁺ ions are implanted in SiO₂ layer of Si wafer at room temperature with the energy 150 keV and with the dose 3×10^{16} ions per cm². Ge clusters are formed within the matrix by neutralization of charges[45].

The PL spectrum of the as-implanted sample is shown in Fig. 9. The PL peaks appear at 562 nm and 656 nm. The first PL peak can be attributed to defect states originated due to implantation process [46], whereas, the second peak can be due to confinement of the electron in oxidized Ge particles of very small size [47]. The detailed discussion on individual components are available in these references. Thus, such studies helps us to search the origin of PL in a system. For PL measurements we first take multiple acquisition for the whole range and then glue the spectra to get the PL spectrum from the sample.

In Fig. 10 the dotted line represents the measured Raman signal from this as-implanted sample. The integration time for this measurement is 300 sec. We have studied confined optic phonons in these Ge nanoparticles and measured the size of the particles from the analysis. The Raman scattering of Ge particles for as-prepared sample shows not only broadening but also asymmetry in line shape with a shift towards low frequency side compared to that

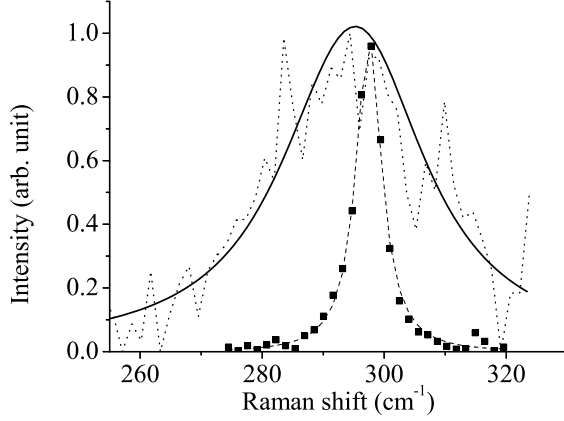


FIG. 10: Raman spectrum from Ge ion implanted Si/SiO₂ sample. The dotted line represents experimental data. The bold line is the fitting of the data with phonon confinement model. *The Raman spectrum of bulk Ge is shown by filled black square in the same graph (with a Lorentzian fitting by dashed line) to clarify the asymmetry and lower frequency shift in the Raman line for the nanoparticles.*

for corresponding bulk materials (Fig. 10). The broadening of the spectra is due to the amorphous nature of Ge clusters in as-implanted sample. The asymmetry arises due to optical phonon confinement. In bulk crystals, the phonon eigenstate is a plane wave and the wavevector selection rule requires $q \approx 0$. In contrast, here the spatial correlation function of the phonon becomes finite due to its confinement in the nanocrystal and hence the $q \approx 0$ selection rule is relaxed [48]. The Raman spectrum $I(\omega)$ due to this confined optic phonon is given by,

$$I(\omega) = A \int \frac{d\mathbf{q} |C(0, \mathbf{q})|^2}{[\omega - \omega(\mathbf{q})]^2 + (\Gamma_0/2)^2} \quad (5)$$

where $\omega(\mathbf{q})$ and Γ_0 are the phonon dispersion curve and the natural line width (FWHM) of the corresponding bulk materials, $C(0, \mathbf{q})$ is the Fourier coefficient of phonon confinement function. *A is an arbitrary constant.* For nanoparticles it has been shown that the phonon confinement function, which fits the experimental data best is $W(\mathbf{r}, L) = \exp\left(\frac{-8\pi^2 r^2}{L^2}\right)$, the square of the Fourier coefficient of which is given by $|C(0, \mathbf{q})|^2 \cong \exp\left(-\frac{q^2 L^2}{16\pi^2}\right)$. L is the size of the particles. The integration in Eqn. 5 must be performed over the whole Brillouin zone [45]. Since the optical phonon dispersion curves are in general not flat, phonon confinement

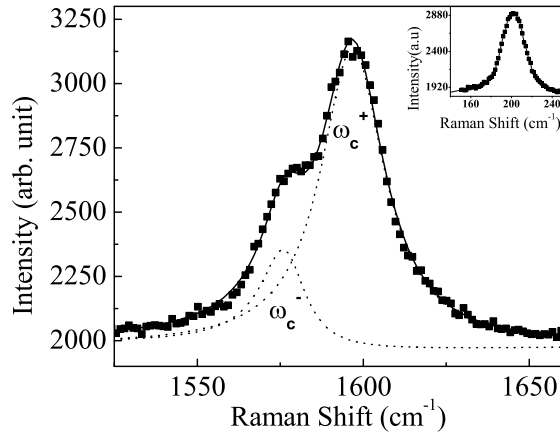


FIG. 11: Dots show vibrational G band of single walled metallic carbon nanotube. The solid line shows the fit using $I(\omega) = I(G^+) + I(G^-)$, a sum of G^+ mode and G^- mode, respectively. The radial mode is shown in the inset

results in a peak shift (usually to lower frequency if frequency is a decreasing function of wavevector in phonon dispersion curve) and asymmetric broadening of the Raman line. Using the above analysis the fitted curve has been shown by the bold line in Fig. 10. The size of the particles, estimated from Raman measurement, is 3.0 ± 0.5 nm. Using Raman and PL measurement simultaneously, we have demonstrated both phonon and electron confinement in Ge nanoparticles embedded in SiO_2 matrix. *It has been shown in the literature that the above defect states are quenched after annealing the sample at 1100 °C for 30 mins. in hydrogen atmosphere [42, 46, 47]. The detail study on our sample with annealing, which reveals the origin of PL in these materials and role of defect states, is beyond the scope of this article and will be reported elsewhere.*

B. One Dimensional System

The Carbon nanotube:

In 1991 Iijima discovered a new allotrope of carbon [49], carbon nanotube, in which the graphite sheets rolled up to form hollow cylinders of few nanometer in diameter but upto a thousand times as long. These nanotubes have revolutionized low dimensional Physics and are utilized extensively in state of art nanoscale research, as mentioned in Section I.

The earliest observations were of micron-long multi walled carbon nanotubes found in the soot by carbon arc method[50]. We have prepared single walled metallic carbon nanotube (SWNT) by thermal decomposition of Acetylene gas in nitrogen atmosphere at 700 °C on porous silicon containing iron particles. Here we demonstrate the capability of our system to characterize milligram quantities of carbon nanotubes. Fig. 11 shows the Raman spectrum of carbon nanotube recorded in our instrument. In this figure, the multi-peak tangential breathing mode (G-band) and low frequency radial mode (in the inset) are the characteristics of metallic single wall carbon nanotube. The Raman-allowed tangential G-mode in graphite is observed at 1582 cm^{-1} . Unlike graphite, the tangential G mode in a nanotube gives rise to multiplex features, known as G-band [51]. An analysis can be carried out considering the two intense features in G-band, which originate from the symmetry breaking of the tangential vibration when the graphite sheet is rolled to make a cylindrical shaped nanotube. The most intense G peak, G^+ band, is for the atomic displacements along the tube axis and G^- band is caused by the curvature of the nanotube, which softens the tangential vibration in the circumferential direction. In Fig. 11 the peak positions for G^+ band and G^- band appear at $1596.8 \pm 0.20 \text{ cm}^{-1}$ (ω_G^+) and $576.8 \pm 0.20 \text{ cm}^{-1}$ (ω_G^-), respectively. For metallic SWNT the G^- band is broadened due to presence of free electrons in nanotubes with metallic character. We have fitted this G^- feature by Briet-Wigner-Fano (BWF) line shape, which is given by

$$I(\omega) = I_0 \frac{[1 + (\omega - \omega_{BWF})/q\Gamma]^2}{1 + [(\omega - \omega_{BWF})/\Gamma]^2} \quad (6)$$

where $-1/q$ is a measure of the interaction of the phonon with a continuum of states and ω_{BWF} is the BWF peak frequency at maximum intensity I_0 [51]. From the fit the value of $-1/q$ has been found to be 0.14, which is close to the value reported in the literature. The higher wavenumber G^+ band has been fitted with Lorentzian line shape. The splitting $\Delta\omega_G = \omega_G^+ - \omega_G^-$ can be used for diameter characterization [52]. In Fig. 11 these two fitted curves are shown by the dotted lines and the net fitted curve is shown by the solid line.

Porous silicon :

The recent observations of highly efficient visible photo- and electro luminescence at room temperature from electrochemically etched porous silicon (PS) have stimulated a lot of excitement mainly due to the possibility of its use in Si-based device application and in designing different sensors [2]. PS has been prepared by electrochemical etching of p-type

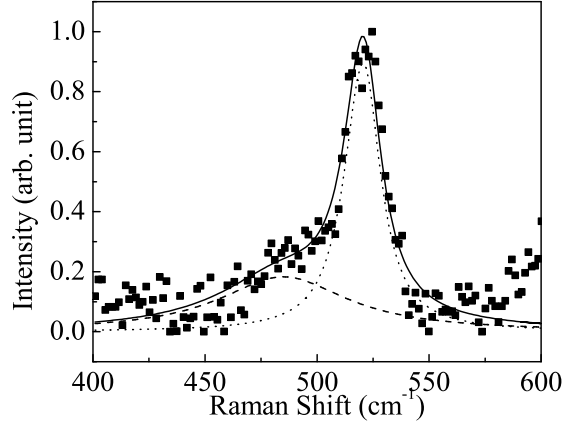


FIG. 12: Dots show the Raman spectrum of as-prepared porous silicon. The solid line shows the fit using $I(\omega) = I_d(\omega) + I_c(\omega)$, a sum of phonon confinement effect (dotted line) and disordered spectrum (dashed line), respectively.

Si wafer of $\langle 100 \rangle$ orientation in 48% HF:ethanol (1:1) solution, keeping current density between 10 and 15 mA/cm². PS can be approximated as quantum wires. Formation of PS on p-type silicon is a self adjusting process due to a geometrical quantum wire effect associated with thin silicon walls remaining between pores after electrochemical etching. A sponge like morphology of PS has been characterized in terms of fractals (an intricate infrastructure consisting of a hierarchy of pores within pores) within certain finite length scale [53]. Both, quantum confinement of electrons in the nanowire and the contribution of defect/disordered states present in this system are important to explain the origin of luminescence in PS [25]. The presence of disordered/amorphous phase has been reported earlier from EPR measurements [54]. Fig. 12 shows the Raman spectrum of PS. Keeping in mind the possibility of presence of disordered/amorphous Silicon (Si) together with the crystalline nanowire of Si, we have fitted the observed line shape with a combined line shape $I(\omega) = I_c(\omega) + I_d(\omega)$, where $I_c(\omega)$ is the confinement Raman line shape (dotted line), given by Eqn. 5 and $I_d(\omega) = B\Gamma_d[\omega - \omega_d]^2 + \Gamma_d^2]^{-1}$ is the Lorentzian line shape (dashed line), which arises due to the disordered/amorphous component. Here ω_d and Γ_d are the phonon frequency and half width at half maximum (HWHM), respectively for the disordered component and B is a constant. The best fit line is shown by the bold line in Fig. 12. In the above exercise of nonlinear least square fit of the data with $I(\omega)$, the fitting parameters

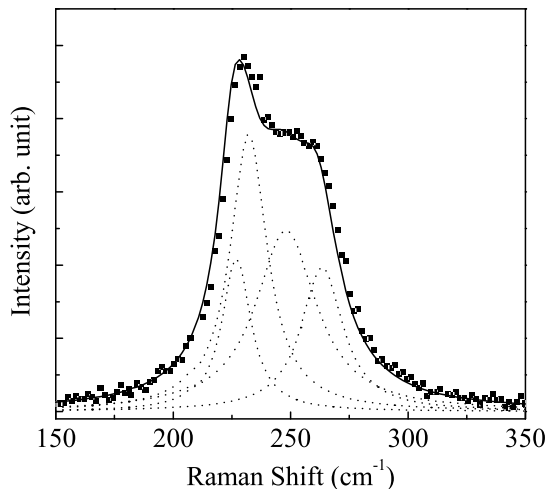


FIG. 13: Raman spectrum of InGaAs 2D layer grown on InP substrate. The dotted lines are four components of LO and TO modes of GaAs and InP. The solid line is the best fit to the data using the above components.

are L , A (both from Eqn. 5), ω_d , Γ_d and B . The phonon dispersion curve for bulk silicon, $\omega(\mathbf{q})$, is taken from Ref.[25]. The diameter of the quantum wire L , estimated from the above Raman analysis, is $40 \pm 5 \text{ \AA}$. Simultaneous PL and Raman measurements on porous silicon can be used to study the origin of PL in this material [25].

C. Two Dimensional System

2D InGaAs quantum layer:

With the rapid development in modern micro/nano electromechanical and VLSI devices it is important to understand the structural and elastic properties of these semiconductor layers[55, 56]. When a superlattice is formed by growing thin layers of materials on a substrate, the differences in their thermal expansion coefficients and lattice constants in these two materials lead to stresses and strains within the layers[57]. Measurement of Raman spectra in these superlattices provides the useful information about the microstrain in semiconductors under stresses [26]. Here we have reported Raman spectrum of as-grown $1\mu\text{m}$ thick $\text{In}_{0.53}\text{Ga}_{0.47}\text{As}$ layer on InP substrate. Thin film $\text{In}_{0.53}\text{Ga}_{0.47}\text{As}$ has been grown on low pressure MOCVD (Metal-Organic Chemical Vapour Deposition) system (CVD Equipment

Corporation) at 629 °C temperature and under a growth pressure of 100 Torr. Flow rate of carrier (H₂) gas was 1.3 lit/min. In this case n⁺ - InP was used as the substrate and 0.5 μm undoped InP buffer layer was grown on it.

In Fig. 13 we have shown Raman spectrum of as-grown In_{0.53}Ga_{0.47}As film on InP substrate. Expecting the presence of both LO and TO modes for InAs and GaAs Raman spectrum between 150 to 270 cm⁻¹ is decomposed into 4 Lorentzians. For the nonlinear least square fit of the data, we have used the FWHM and peak intensities as free fitting parameters. The peak positions are kept within ± 5 cm⁻¹ of the bulk LO and TO phonon modes for GaAs and InAs. Peak A appears between 226.7 cm⁻¹ and 229.4 cm⁻¹ (InAs-like TO mode), peak B - at 241.5 cm⁻¹ (InAs-like LO mode), peak C - at 254.3 cm⁻¹ (GaAs-like TO mode) and peak D between at 266.0 cm⁻¹ (GaAs-like LO mode). In the above fitting procedure it is difficult to comment on Raman shift of peak B and C distinctly, as they are very close to each other. We have estimated the stress within the layers from the shift in Raman peak positions of GaAs-like longitudinal optical (LO) phonons in the systems. Though at room temperature In_{0.53}Ga_{0.47}As/InP is almost perfectly lattice matched, at the growth temperature (629°C), In_{0.53}Ga_{0.47}As has a lattice constant less than that of InP and the layer is under compression [58]. GaAs-like Raman mode for lattice matched In_{0.53}Ga_{0.47}As/InP appears at 270 cm⁻¹ [26]. The phonon frequencies of the same mode in our samples, as obtained by fitting the Raman spectrum is 266.0 ± 0.56 cm⁻¹. The shift in the Raman line from its value in lattice matched sample can be attributed to the biaxial stress in the film due to lattice mismatch. Following [26] & [58] the frequency of the optical phonons in the presence of biaxial stress can be expressed by

$$\Omega_{LO} = \Omega_{LO}^0 - \eta_H \sigma - \frac{2}{3} \eta_S \sigma \quad (7)$$

where Ω_{LO}^0 is the phonon frequency without stress and

$$\eta_H = -(p + 2q)(S_{11} + S_{12})\Omega_0/6\omega_0^2 \quad (8)$$

and

$$\eta_S = (p - q)(S_{11} - S_{12})\Omega_0/2\omega_0^2 \quad (9)$$

Here S_{11} and S_{12} are the elastic stiffness constants, p and q are the optical deformation

| Ω_0 (s ⁻¹) | $S_{11} + 2S_{12}$ (Pa ⁻¹) | $S_{11} - S_{12}$ (Pa ⁻¹) | $(p+2q)/6\omega_0^2$ | $(p-q)/2\omega_0^2$ |
|-------------------------------|--|---------------------------------------|----------------------|---------------------|
| 0.511×10^{14} | 0.445×10^{-11} | 1.54×10^{11} | 0.2 | -0.1 |

TABLE II: Elastic stiffness constant, optical deformation constant for InGaAs

constants. In above Eqns 8 & 9, optical phonon frequency, Ω , is in unit of cm⁻¹ and ω_0 is in sec⁻¹. The values of $p + 2q$, $p - q$, $S_{11} + 2S_{12}$ and $S_{11} - S_{12}$, ω_0 , are tabulated in Table 2 (from [26]). In above Eqns 8 & 9, Ω s are in unit of cm⁻¹ and ω_0 is in sec⁻¹. The compressive stress in the film is then given by the expression

$$\sigma = -0.4\partial\Omega_{LO}GPa \quad (10)$$

where $\partial\Omega_{LO} = \Omega_{LO}^0 - \Omega_{LO}$. σ is positive for tension and negative for compression. The stresses within the layers in the samples, estimated from the Raman measurements, is 1.6 ± 0.2 GPa.

VI. CONCLUSION

The ability to control, manipulate and design materials in the nanometer scale is one of the major technology drivers of the 21st century. Thus, to use these materials one needs to understand their basic physical properties in details. We have described design and fabrication of a low-cost spectrometer with home-built collection optics for advanced research projects, specially ideal to study optical and vibrational properties of nanomaterials. The low cost open electrode CCD detector enables us to acquire weak signals with large integration time. High throughput of a single stage Monochromator also helps us to detect very weak signals from nanomaterials. The system can be easily modified to a MicroRaman set-up, with a microscope attachment.

To establish the performance of our instrument for studying present state of art materials we have worked on 0D system (Ge nanoparticles), 1D system (Si nanowire, Carbon nanotube) and 2D system (InP-InGaAs thin film). The spectrometer could successfully record very weak Raman signal from these samples. Different techniques to analyze the data to get useful information about the sample have been briefly described in this article. Using same set-up we could also measure PL from the samples. Simultaneous PL and Raman measurements are important to study these new materials. PL experiments help in understanding

the nature of luminescent states, whereas Raman scattering probes the underlying quantum network.

A wide range of studies can be performed using the same instrument. For example, Surface Enhanced Raman Scattering (SERS) [59] is a useful technique resulting in strongly increased Raman signals from molecules, which have been attached to nanometer scale metallic structure. It is an unique technique to probe individual molecules. Our spectrometer is capable of carrying out this single molecule spectroscopy. To begin with, we have probed molecular vibrations in single molecule of methylene blue dye absorbed on silver sol by SERS.

To conclude, we have described a set-up for Raman and PL measurements, which can be ideally used in research as well as in any graduate level course on nanomaterials, where the importance of spectroscopic investigation is adequately emphasized. Through the differences that arise in the spectroscopic effects, we can mark and measure the unique features inherent to the nanostructures within the sample. The examples provided in this article illustrate quite clearly how our Raman PL set-up can efficiently probe the nano -aspects, so important in modern-day technology. We hope that this article will motivate researchers to make use of our set-up for appropriate purposes in future.

VII. ACKNOWLEDGEMENTS

AR thanks Department of Science and Technology (DST) in India for financial support and Dr. S. Kar for fruitful suggestions and discussions. Authors thank Nuclear Science Centre, Delhi, India, for help in preparing the Ge implanted SiO₂ sample, Prof. D.N. Bose for MOCVD grown InGaAs quantum well sample and M.S. Morrison for technical help with the set-up.

-
- [1] M. Han, X. Gao, J. Z. Su and S. Nie, “Quantum-Dot-tagged microbeads for multiplexed optical coding of biomolecules,” *Nat. Biotech* **19**, 631 (2001).
 - [2] K. D. Hirschman, L. Tsybeskov, S. P. Dutttagupta and P. M. Fauchet, “Silicon-based visible light-emitting devices integrated into microelectronic circuits,” *Nature* **384**, 338 (1996).

- [3] P. G. Collins, M. S. Arnold and P. Avouris, "Engineering carbon nanotubes and naotube circuits using elctrical breakdown," *Science* **292**, 706 (2001).
- [4] S. Ghosh, A. K. Sood and N. Kumar, " Carbon nanotube flow sensors," *Science* **299**, 1042 (2003).
- [5] M. Ouyang, J. L. Huang, C. L. Cheung and C. M. Lieber, "Atomically resolved single-walled carbon nanotube intramolecular junctions," *Science* **291**, 97 (2001).
- [6] H. Ahmed and K. Nakazato, "Single-electron devices," *Microelectronic Engineering* **32**(1-4), 297 (1996).
- [7] C. E. Grethlein, *A look inside nanotechnology* (DOD Researchers provide AMPTIAC Quarterly Ed., Vol. **6**, (2002).
- [8] C. Chen, M. Khobaib and D. Curliss, "Epoxy layered-silicate nanocomposites," *Prog. in Org. Coatings* **47**, 376 (2003).
- [9] A. Smekal, *Naturwissenschaften* **11**, 873 (1923).
- [10] C. V. Raman and K. S. Krishnan, "A new type of secondary radiation," *Nature* **121**, 501 (1928).
- [11] Lord Rayleigh and J. W. Strutt, "On the transmission of light through an atmosphere containing small particles in suspension and on the origin of blue sky," *Phil. Mag.* **47**, 375 (1899).
- [12] W. Hayes and R. Loudon, *Scattering of light by crystals* (John Wiley & Sons, New York, 1978).
- [13] M. Cardona and G. Güntherodt, *Light scattering in solids II - Basic concepts and Instrumentation* (Springer-Verlag, Berlin, 1982).
- [14] R. Loudon, "Raman Effect in crystals," *Adv. in Phys.* **13**, 423 (1964).
- [15] H. Lamb, *Proc. in London Math.* "On the vibrations of an elastic sphere," Vol.13, p.187,1882.
- [16] E. Duval, A. Boukenter and Champagnon, "Vibration eigenmodes and size of microcrystallites in glass: observation by very- low-frequency Raman scattering," *Phys. Rev. Lett.* **56** (19), 2052 (1986); M. Fujii, T. Nagareda, S. Hayashi and K. Yamamoto, "Low-frequency Raman scattering from small silver particles embedded in SiO₂ thin films," *Phys. Rev.* **B44** (12), 6243 (1991)
- [17] A. Roy and A. K. Sood, "Growth of CdS_xSe_{1-x} nanoparticles in glass matrix by isochronal thermal annealing : Confined acoustic phonons and optical absorption studies," *Solid State Commun.***97**(2), 97 (1996).

- [18] C. Colvard, T.A. Gant, M.V. Klein, R. Merlin, R. Fischer, H. Morkoc and A.C. Gossard, “Folded acoustic and quantized optic phonons in (GaAl)As superlattices,” *Phys. Rev.* **B31**(4), 2080 (1985).
- [19] S.M. Rytov, *Sov. Phys. Acoust.* **2**, 68 (1956).
- [20] A. K. Sood, “Phonons in semiconductor superlattices,” *Def. Sci J* **39**(4),411 (1989) and the references therein.
- [21] R. Fuchs and K. L. Kliewer, “Optical modes of vibrations in an ionic crystal sphere,” *J. Opt. Soc. Am* **58** (3), 319 (1968).
- [22] A. Roy and A. K. Sood, “Surface and confined optical phonons in $\text{CdS}_x\text{Se}_{1-x}$ nanoparticles in a glass matrix,” *Phys. Rev.* **B53** (18), 12127 (1996).
- [23] T. Ruf, *Phonon Raman-Scattering in Semiconductors, Quantum Wells and Superlattices : Basic Results and Applications* (Springer Verlag, Springer Tracts in Modern Physics. Vol. 142, 1998).
- [24] D. S. Jiang, X. P. Li, B. Q. Sun and H. X. Han, “A Raman scattering study of GaAs: As films lifted off GaAs substrate,” *J Phys D, Appl. Phys.* **32** (6), 629 (1999);
- [25] A. Roy, K. Jayaram and A. K. Sood, “Raman and Photoluminescence studies of thermally annealed porous silicon,” *Solid State Commun.* **89** (3), 229 (1994).
- [26] F. Cerderia, C. J. Buchenauer, F. H. Pollak and M. Cardona, “Stress-induced shifts of first-order Raman frequencies of diamond- and zinc-blende-type semiconductors,” *Phys. Rev.* **B5**(2), 580 (1972).
- [27] E. Liarokapis, D. Papadimitriou, J. Rumberg and W. Richter, “Raman and RAS measurements on Uniaxially strained Thin Semiconductor Layers,” *Phys. Stat. Sol. (b)* **211**, 309 (1999).
- [28] J. Karpinski, J. Jun, S. Porowski, “Equilibrium pressure of N_2 over GaN and high pressure solution growth of GaN” *J. Cryst. Growth* **66**, 1 (1984); H. W. Kunert, “Raman selection rules in C_{6v}^4 hexagonal crystals:allowed combination and overtone of vibrational modes in wurtzite GaN,” *Cryst. Res. Technol.* **38** (3-5), 366 (2003).
- [29] F. Decremps, J. Plicier-Porres, A. Marco Saitta, J. C. Chervin and A. Polian, “High-pressure Raman spectroscopy study of wurtzite ZnO,” *Phys. Rev* **B65**, 092101 (2002).
- [30] N. Chandrabhas and A. K. Sood, “Raman study of pressure-induced phase transitions in RbIO_4 ,” *Phys. Rev.* **51B** (14), 8795 (1995). 999

- [31] P.Moriarty, “Nanostructured Materials,” Rep. Prog. Phys **64** (3), 297 (2001) and the references therein.
- [32] T. S Kim, S. D Lester and B.G. Streetman, “Photoluminescence study of heat-treated InP,” J. Appl. Phys. **61** (9), 4598 (1967).
- [33] S. D. Lester, T. S. Kim and B. G. Streetman, “Factors Influencing the photoluminescence Intensity of InP,” J. Electrochem Soc **133** (10), 2208 (1986).
- [34] T. S. Kim, S. D. Lester and B. G Streetman, “Observation of radiative surface states on InP,” J Appl Phys **61** (5), 2072 (1987).
- [35] H. B. Bebb and E. W. Williams, *Semiconductors and Semimetals* (R. K. Williamsons, A. C. Beer, editors, Elsevier, vol. 8, p. 181, 1975).
- [36] R. Voor, L. Chow and A. Schulte, “MicroRaman spectroscopy in the undergraduate research laboratory, ” Am. J. Phys. **62**(5), 429 (1994).
- [37] Spectrmax is a trademark of Instrument SA, Inc. USA for Window OS.
- [38] H. Bliz and W. Kress, *Phonon dispersion relations in insulators* (Springer Verlag, p. 97, 1979); also see Reference [2] p.63 & p.143.
- [39] P. Grassmann and J. Weiler Z. Phys; **86**, 321 (1933).
- [40] A. I. Ekimov and A. A. Onushchenko, “Quantum size effect in the optical spectra of semiconductor microcrystals,” Sov. Phys. Semicond. **16** (7), 775 (1982); A. I Ekimov, Al. L. Efros and A. A. Onushchenko, “Quantum size effect in semiconductor microcrystals,” Solid State Commun. **56** (11), 921 (1985).
- [41] L. Brus, “Zero-dimensional “excitons” in semiconductor clusters,” IEEE J. Quant. Electron. **22** (9), 1909 (1986).
- [42] Y. Maeda, N. Tsukamoto, Y. Yazawa, Y. Kanemitsu and Y. Masumoto, “Visible photoluminescence of Ge microcrystals embedded in SiO₂ glassy matrices,” Appl. Phys. Lett. **59** (24), 3168 (1991).
- [43] T. Shimizu-Iwayama, M. Oshima, T. Niimi, S. Nakao, K. Saitoh, T. Fujita and N. Itoh, “Visible photoluminescence related to Si precipitates in Si⁺- implanted SiO₂,” J. Phys. Cond. Mat. **5**, L375 (1993).
- [44] J.von Borany, R. Grötzschel, K. H. Heinig, A. Markwitz, B. Schmidt, W. Skorupa and H. -J. Thees, “The formation of narrow nanocluster bands in Ge-implanted SiO₂-layers,” Solid State Electron. **43**, 1159 (1999).

- [45] M. Yamamoto, T. Koshikawa, T. Yasue, H. Harima and K. Kajiyama, "Formation of size controlled Ge nanocrystals in SiO₂ matrix by ion implantation and annealing," *Thin Solid Films* **369**, 100 (2000).
- [46] H. B. Kim, K. H. Chae, C. N. Whang, J. Y. Jeong, M. S. Oh, S. Im and J. H. Song, "The origin of photoluminescence in Ge-implanted SiO₂ layers," *J. Lumin.* **80**, 281 (1999); K. S. Min, K. V. Shcheglov, C. M. Yang and H. A. Atwater, "The role of quantum-confined excitons vs defects in the visible luminescence of SiO₂ films containing Ge nanocrystals," *Appl. Phys. Lett.* **68** (18), 2511 (1996).
- [47] S. Okamoto and Y. Kanemitsu, "Photoluminescence properties of surface-oxidized Ge nanocrystals: Surface localization of excitons," *Phys. Rev.* **B54** (23), 16421 (1996).
- [48] I. H. Campbell and P. M. Fauchet, "The effects of Microcrystal size and shape on the one phonon Raman spectra of crystalline semiconductors," *Solid State Commun* **58** (10), 739 (1986).
- [49] S. Iijima, "Helical microtubules of graphitic carbon," *Nature* **354**, 56 (1991).
- [50] W. Krätschmer, L. D. Lamb, P. Fostiropoulos and D. R. Huffman, "Solid C₆₀ : a new form of carbon," *Nature* **347**, 354 (1990).
- [51] S. D. M. Brown, A. Jorio, P. Corio, M. S. Dresselhaus, R. Saito and K. Kneipp, "Origin of Breit-Wigner-Fano lineshape of the tangential G-band feature of metallic carbon nanotubes," *Phys. Rev.* **B63**, 155414 (2001).
- [52] A. Jorio, M. A. Pimenta, A. G. Souza Filho, R. Saito, G. Dresselhaus and M. S. Dresselhaus, "Characterizing carbon nanotube samples with resonance Raman scattering," *New J. Phys.* **5**, 139.1 (2003).
- [53] S.F. Chuang, S.D. Collins and R.L. Smith, "Porous silicon microstructure as studied by transmission electron microscopy", *Appl. Phys. Lett.* **55**, 1540 (1989); A. Roy and A.K. Sood, "Fracton dimension of porous silicon as determined by low-frequency Raman scattering", *Solid State. Commun.* **93**(12), 995 (1995).
- [54] S.M. Prokes, W.E. Carlos and V.M. Bermudez, "Luminescence cycling and defect density measurements in porous silicon: Evidence of hydride based model", *Appl. Phys. Lett.* **61**, 1447 (1992).
- [55] M. Oishi, M. Yamamoto and K. Kasaya, "2.0- μ m single-mode operation of InGaAs-InGaAsP distributed-feedback buried-heterostructure quantum-well lasers," *IEEE Photonics Technol.*

- Lett. **9**(4), 431 (1997).
- [56] M. Ochiai, H. Temkin, S. Forouhar and R. A Logan, "InGaAs-InGaAsP buried heterostructure lasers operating at $2.0\ \mu\text{m}$," IEEE Photonics Technol. Lett. **7** (8), 825 (1995).
- [57] F. H. Pollak, *Proc. of the Tenth International Conference on the Physics of Semiconductor* (Cambridge, U.S Atomic Energy Commision, Oak Bridge, Tenn. p. 407, 1970).
- [58] T. Yagi, Y. Fujiwara, T. Nishino and Y. Hamakawa, "Photoluminescence and Lattice Mismatch in InGaAs/InP," Jpn. J. Appl. Phys. **22** (7), L467 (1983).
- [59] K. Kneipp, Y. Wang, H. Kneipp, L. T. Perelman and I. Itzkan, "Single molecule detection using surface-enhanced Raman scattering (SERS)," Phys. Rev. Lett. **78** (9) 1667 (1997).